Field-programmable ring array employing AMZI-assisted-MRR structure for photonic signal processor

Yaohui Sun ; Dongyu Wang ; Lihan Wang ; Yue Zhou ; Shilong Pan ; Guohua Hu ✉ ; Binfeng Yun ; Yiping Cui

Check for updates

View Online

Export Citation

Field-programmable ring array employing AMZI-assisted-MRR structure for photonic signal processor

View Online　Export Citation　CrossMark

Yaohui Sun,[1] 　Dongyu Wang,[1] 　Lihan Wang,[2] 　Yue Zhou,[1] 　Shilong Pan,[2] 　Guohua Hu,[1,a]
Binfeng Yun,[1] 　and Yiping Cui[1]

AFFILIATIONS

[1] Advanced Photonics Center, School of Electronic Science and Engineering, Southeast University, Nanjing 210096, People's Republic of China

[2] Key Laboratory of Radar Imaging and Microwave Photonics, Ministry of Education, Nanjing University of Aeronautics and Astronautics, Nanjing 210016, People's Republic of China

[a] Author to whom correspondence should be addressed: photonics@seu.edu.cn

ABSTRACT

A field-programmable photonic gate array is an integrated optical chip that combines electrical control and optical processing, enabling real-time reconfiguration of the optical path through software programming. While most current optical processors rely on Mach–Zehnder interferometer (MZI)-based architectures, those based on micro-disk resonators (MDRs) offer unique characteristics, including high integration and wavelength correlation, providing new ideas for programmable photonic chip architectures. In this paper, a scalable asymmetric MZI-assisted field-programmable micro-ring array (AMZI-FPRA) processor is proposed with a cell area of only $85 \times 42 \, \mu m^2$. This design not only has high wavelength selectivity but also possesses dual adjustable wavelengths and coupling coefficients compared with traditional MDRs. By extending the cell into a 2×2 AMZI-FPRA using a two-dimensional square mesh approach, it is experimentally demonstrated that different optical path topologies can be realized with a compact footprint, including bandpass bandstop filtering, optical temporal differentiation, microwave delay, wavelength-division multiplexing/demultiplexing, and optical add-drop multiplexing. Increasing the array scale will enable more versatile and high-performance microwave photonic signal processing tasks. The scheme will be a promising candidate at the present time for reconfigurable programmable photonic signal processors due to its wide reconfigurability, on-chip integration, complementary metal–oxide–semiconductor-compatibility, and low power consumption.

I. INTRODUCTION

The tremendous development of digital data generated from social media, the Internet of Things, high-definition images, and videos has powerfully stimulated the rapid advance of big data territory. To satisfy the demand for ever-increasing communication capacity and high-speed signal processing, widespread utilization of high-performance integrated circuits is widely applied, especially field-programmable gate arrays (FPGAs), which possess the uniqueness of fast reconfigurability.[1,2] However, due to intrinsic restrictions imposed by electronic bottlenecks,[3] traditional electronic processing encounters limitations in terms of computation speed and power efficiency, even in the state-of-the-art FPGA. In particular,

all-optical processing featuring ultra-fast computation speed, ultra-wide bandwidth, and low power consumption[4–7] has been envisaged as a promising technology for data operation and calculation.[8,9] Based on this scheme, considerable progress has been made in successfully implementing photonic-assisted signal processors.[10–12] Nevertheless, the practicability and cost-effectiveness of these solutions are greatly restricted by their reliance on discretized optical fiber components or devices.

In recent years, numerous studies have been devoted to the development of photonic-integrated circuits (PICs) for on-chip photonic signal processors.[13–16] Various fixed-frame schemes have been proposed and demonstrated based on different material platforms[17–20] and guided by multi-objective tasks.[21–26] However,

in the actual application scenario, there is a significant need for a general photonic signal processor that can be reconfigured according to requirements, such as an FPGA-based signal processor. Currently, Mach–Zehnder interferometers (MZIs) have achieved a dominant position as fundamental building blocks of programmable signal processors owing to their wide bandwidth, high processing tolerance, and flexible optical routing ability.[9,27–32] Although the MZIs are not directly employed in several proposals,[33–36] they are introduced to realize or improve the reconfigurability and programmability of the overall device. Obviously, these MZI-based solutions require a large footprint, which limits their integration into a compact framework and hinders their scalability. Several alternative fundamental candidates are presented, including multi-mode interferometers (MMIs),[37] dual-drive directional couplers (DD-DC),[38] nanobeam structures,[39,40] and multi-port directional couplers (MDCs)[41] for better compactness and lower insertion losses as key components for performing unitary transformations. However, they are insufficient replacements for MZI-based solutions according to their functional expression and performance index. More compact blocks, represented by micro-ring resonators (MRRs)[42,43] and micro-disk resonators (MDRs),[44] have also been researched for programmable photonic signal processors, achieving great success in unique processing types and modes for their integration and wavelength selectivity.[45,46]

In parallel, the tunable parameters of conventional micro-ring or micro-disk resonator structures are generally limited to only the resonance wavelength. The resonance state of an MRR is extremely dependent on fabrication precision and can hardly be adjusted after manufacturing, resulting in a deviation between actuality and simulation. It has been reported that by replacing the coupling region of the MRR[23–25,47] with tunable MZI couplers, the reconfigurability of these devices is significantly improved. However, as a result of the large size of the MZIs, both the length and the loss of the overall ring increase, leading to a reduction in the free spectral range (FSR) as well as degradation in the extinction ratio and quality factor. Moreover, controlling resonance states and wavelengths interact with each other, causing noticeable wavelength shifts while tuning the coupling coefficient. This phenomenon indicates the complexity and difficulty associated with tuning these devices. In 2017, Dong *et al.* proposed an optical temporal differentiator using an asymmetric MZI-assisted MRR structure instead of conventional coupling regions.[48] By introducing this asymmetric MZI structure without substantial expansion of the footprint, it becomes possible for the coupling coefficient to vary within a certain range. This approach greatly improves tunability since the control of the resonance states and resonance wavelengths is mutually independent. Furthermore, this technique has been applied in optical pulse processing[49] as well as high-spectral-purity photon generation.[50]

In this work, we report a scalable photonic integrated field-programmable ring array employing asymmetric MZI-assisted MRR, abbreviated to AMZI-FPRA, based on a silicon-on-insulator (SOI) platform for further exploration of promising architectures
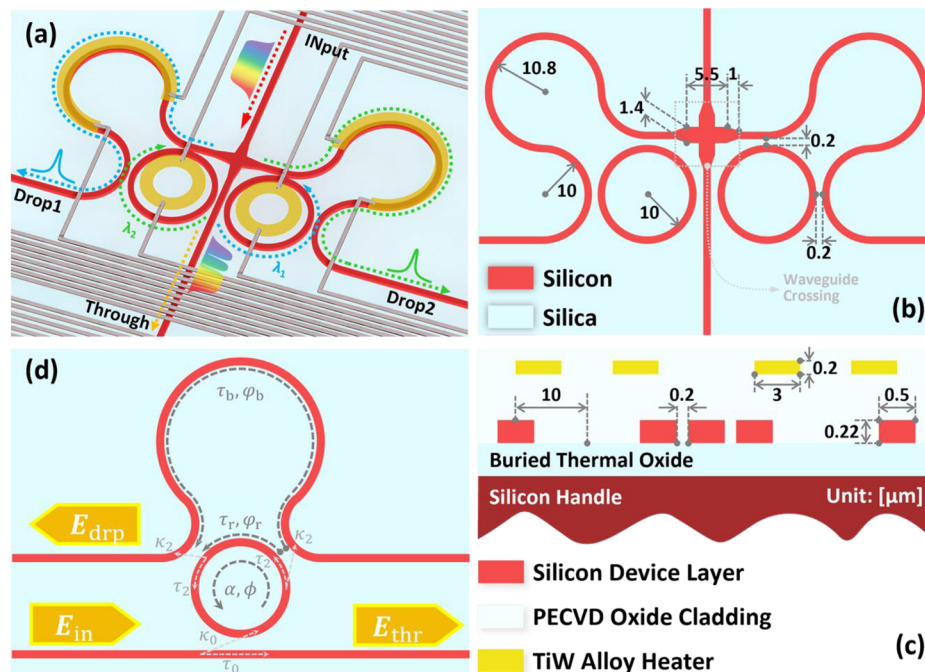
FIG. 1. AMZI-FPRA cell. (a) Zoom-in view of the fundamental cell of the proposed AMZI-FPRA signal processor. (b) Top view of the fundamental cell with key dimension parameters. (c) Cross-sectional view of the planar structure of two rings. (d) Schematics of the AMZI-MRR structure.

for high-density integrated and field-programmable PICs. Utilizing the flexibility of both asymmetric MZIs and MRRs, the fundamental execution cell exhibits outstanding tunability in resonance wavelength and coupling coefficient. This significantly enhances the diversity of functions and the tunability of performance while maintaining a compact footprint and low-power consumption suitable for ultra-fast and reconfigurable signal processing. We have experimentally verified the compactness and flexibility of the cell in performing various optical operations. Moreover, using a fabricated 2 × 2 AMZI-FPRA, we have demonstrated several photonic microwave signal-processing functions, including frequency-tunable bandpass filtering, flat-top and Fano-like filtering, bandstop filtering, multi-channel temporal differentiation, tunable microwave delay, reconfigurable wavelength division (WDM) (de)multiplexing, and optical add-drop multiplexing (OADM). With the extension of the array scale, additional functionalities can be achieved. There are great prospects for future applications in field-programmable photonic computing and signal processing.

II. OPERATION PRINCIPLE AND PERFORMANCE OF THE CELL BASED ON AMZI-MRR

A. Operation principle of the cell

The schematic diagram of the proposed fundamental cell is illustrated in Fig. 1(a), in which the single micro-ring can be extracted as an add-drop MRR, as shown in Fig. 1(c). The frequency response of an add-drop MRR at the through port and drop port can be expressed as

$$\frac{E_{\text{thr}}}{E_{\text{in}}} = \frac{\tau_0 - \alpha\tau_1 e^{j\phi}}{1 - \alpha\tau_0\tau_1 e^{j\phi}},$$

$$\frac{E_{\text{drp}}}{E_{\text{in}}} = \frac{\kappa_0\kappa_1 e^{\frac{j\phi}{2}}}{1 - \alpha\tau_0\tau_1 e^{j\phi}},$$

(1)

where α represents the round-trip intrinsic loss of the ring resonator, κ_0 and κ_1 are the cross-coupling coefficients for the input waveguide and add waveguide, and τ_0 and τ_1 are the self-coupling coefficients for their respective positions. ϕ denotes the round-trip phase shift of the ring resonator. According to Fig. 1(d), by introducing an asymmetric MZI (AMZI) to replace an original coupling region, we obtain an equivalent cross-coupling coefficient of the AMZI is

$$\kappa_1 = \kappa_2(1 - \kappa_2) \cdot \left[\tau_b + \tau_r - 2\sqrt{\tau_b\tau_r}\cos(\varphi_b - \varphi_r)\right],$$

(2)

where κ_2 represents the cross-coupling coefficient between MZI arms and the micro-ring. τ_b, τ_r, φ_b, and φ_r are the transmission coefficients and phase shifts of the MZI arm and ring arm, respectively. Assuming a lossless coupling process, the equivalent self-coupling coefficient satisfies $\tau_1^2 + \kappa_1^2 = 1$.

As shown in Fig. 1(a), micro-heaters are added to cells to achieve tunability based on the thermo-optic effect of the silicon. Since the three-waveguide coupling region within each cell depends on a traditional directional coupling structure with fixed cross-coupling coefficients after fabrication, the depth of the notch and
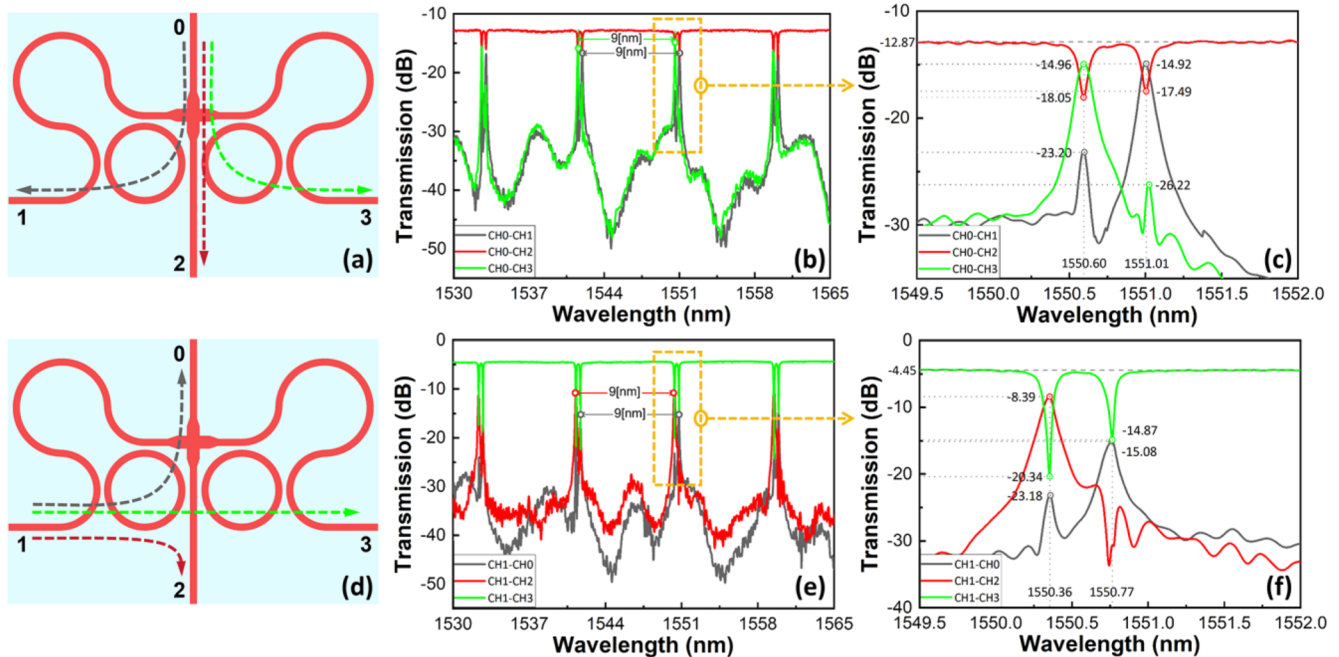
FIG. 2. (a) The port description of the AMZI-FPRA cell and a schematic diagram of the optical path with port 0 as the input. (b) Measured transmission spectrum and (c) detail enlargement at port 0 of the four-port cell with the FSR of 9 nm. (d) The schematic diagram of the optical path with port 1 as the input. (e) Measured transmission spectrum and (f) detail enlargement at port 1 of the cell.

the coupling state can be adjusted by controlling the heating power of the micro-heaters upon the AMZI arms. The micro-heaters above the micro-ring enable adjustment of the resonant wavelength. Different from a single tunable parameter such as resonance wavelength typically associated with a micro-ring or micro-disk, the proposed AMZI-assisted micro-ring possesses dual-tunability characterized by both resonance wavelength and resonance state adjustments. This dual-tunability feature enables compensation for potential manufacturing errors, ensuring reliable device utilization.

Attributed to the high index contrast and compatibility with complementary metal–oxide–semiconductor (CMOS) technology, the proposed processor is fabricated on the SOI platform, which offers advantages such as compactness and seamless integration with electronics. Figure 1(b) displays the top view of a fundamental cell within the AMZI-FPRA. Within the MZI-assisted MRR, the radius of the MRR is 10 μm, while the total length of the AMZI arm is 82.31 μm. The coupling gap between the AMZI arm and the ring resonator is 200 nm. To guide optical signals at the waveguide intersections, we employ a low-loss and low-crosstalk compact waveguide crossing based on a 1×1 multi-mode-interferometer

(MMI) configuration, whose specific parameters are also exhibited in Fig. 1(b). The effective area of each cell is $85 \times 42 \ \mu m^2$. According to Fig. 1(c), the section size of the waveguide is $500 \times 220 \ nm^2$, while the section size of the TiN alloy micro-heater is $3 \ \mu m \times 200 \ nm$. The gaps between rings and waveguide crossings have widths of 200 nm for the resonance state, changing from an under-coupling state to an over-coupling state.

B. Experimental performance of the cell

A broadband light source is utilized to examine the spectral transmission of the cell. Figure 2 illustrates the transmission spectra with a wavelength range of 1530 to 1565 nm. Different ports are selected to observe variations in the spectral response. Regardless of the input port selection, the FSR of the cell remains at 9 nm. Despite sharing identical parameters for ring radii and the coupling gaps, there exists a separation in resonance wavelengths between two rings owing to asymmetric phase jumps at the three-waveguide-coupling region. Comparing Figs. 2(b) and 2(e), a similarity of the spectra out of the resonance wavelengths can be seen more clearly in Fig. 2(b).
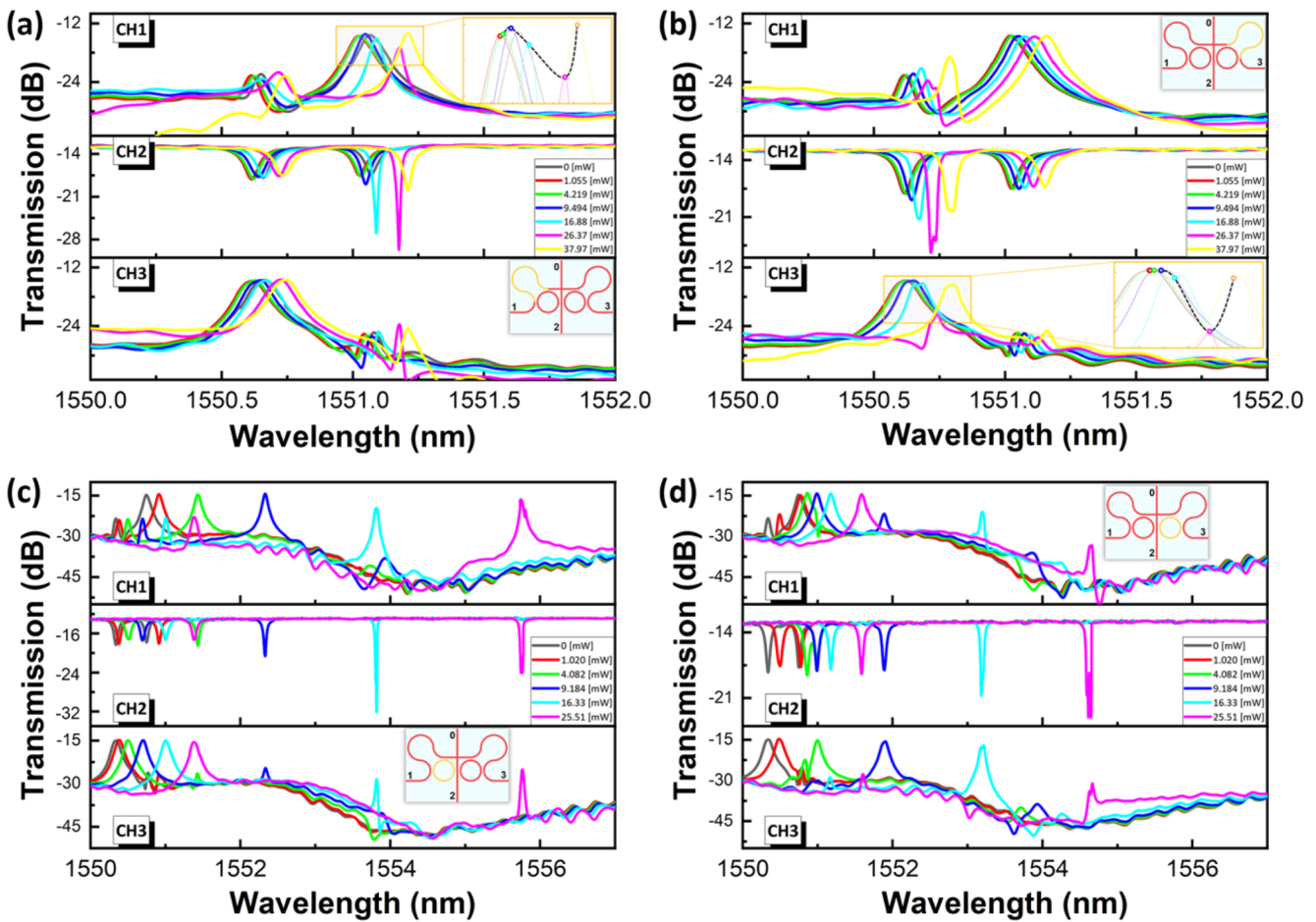

FIG. 3. Spectral changes of each output port after tuning on (a) left AMZI arm, (b) right AMZI arm, (c) left ring, and (d) right ring, which are marked yellow in the top view.

17 June 2024 12:43:05

By enlarging the details as shown in Fig. 2(c), notch depths at port 2 measure −18.05 and −17.49 dB, respectively, while corresponding peaks reach −14.96 and −14.92 dB, indicating good consistency between outputs from both drops. However, there is a significant peak difference between drops in Fig. 2(f), reaching up to 6.69 dB, which severely affects the functional representation of one ring by another ring's output signal interference. In addition, as exhibited by Fig. 2(c), a secondary peak emerges at the drop port, where its resonance wavelength aligns with that of the primary peak observed at another drop port, which serves as the main source of the crosstalk. Comparatively, Fig. 2(f) exhibits less trouble with crosstalk. Considering the superior performance offered by this array architecture, we have selected input from port 0 for subsequent experiments.

By adjusting the heating electrodes at corresponding positions, the spectra of the three ports can be modified accordingly. As shown in Figs. 3(a) and 3(b), controlling the resonance states of the corresponding ring by heating the AMZI arm leads to noticeable fluctuations in both the notch and the peak features. The resonance wavelength is also shifted due to thermal effects. Moreover, although only intended for tuning the resonance state of a micro-ring, there is a slight shift of ~0.19 nm observed in its corresponding micro-ring when reaching a heating power of 37.97 mW, primarily attributed to thermal crosstalk. Since the shifts are so small, they are neglected in practical applications. A similar phenomenon is observed during resonance wavelength tuning as well. Altering one ring's resonance wavelength causes a certain extent of shifting (around 1.02 nm with a heat power level of 25.51 mW) in the other ring's resonance wavelengths. Although the temperature control system has been loaded, it

is still limited in suppressing localized thermal gradients and, therefore, cannot completely eliminate thermal crosstalk. Nevertheless, considering that more attention is focused on relative positions, this wavelength shift caused by thermal crosstalk can be neglected in comparison with the change in relative positions. Based on the validation of the basic functionality of the cell design, we further investigate extending this single cell into an AMZI-FPRA processor in the subsequent chapters.

III. EXPERIMENTAL RESULTS AND DISCUSSION OF THE 2 × 2 AMZI-FPRA PROCESSOR CHIP

A. Chip fabrication and experiments

To verify the basic functionality of the processor chip, a 2 × 2 AMZI-FPRA processor chip was fabricated and produced, containing only four cells. Figure 4(a) depicts the schematic diagram of the proposed 2 × 2 AMZI-FPRA processor chip. As illustrated, the cascaded extension enables a broader range of functionalities for the entire chip. The micrograph displayed in Fig. 4(b) shows the chip's actual structure. The chip is based on a conventional SOI platform with a 220 nm-thick silicon device layer and a 2 μm-thick buried thermal oxide layer. The device was manufactured using electron-beam direct patterning and anisotropic inductively coupled plasma reactive ion etching (ICP-RIE) processes with an etching depth of 220 nm. To ensure thermal and optical isolation, a plasma-enhanced chemical vapor deposition (PECVD) process was employed to deposit an oxide cladding layer on the top of the silicon layer, with a thickness of 2.2 μm. The routing layer for electrical
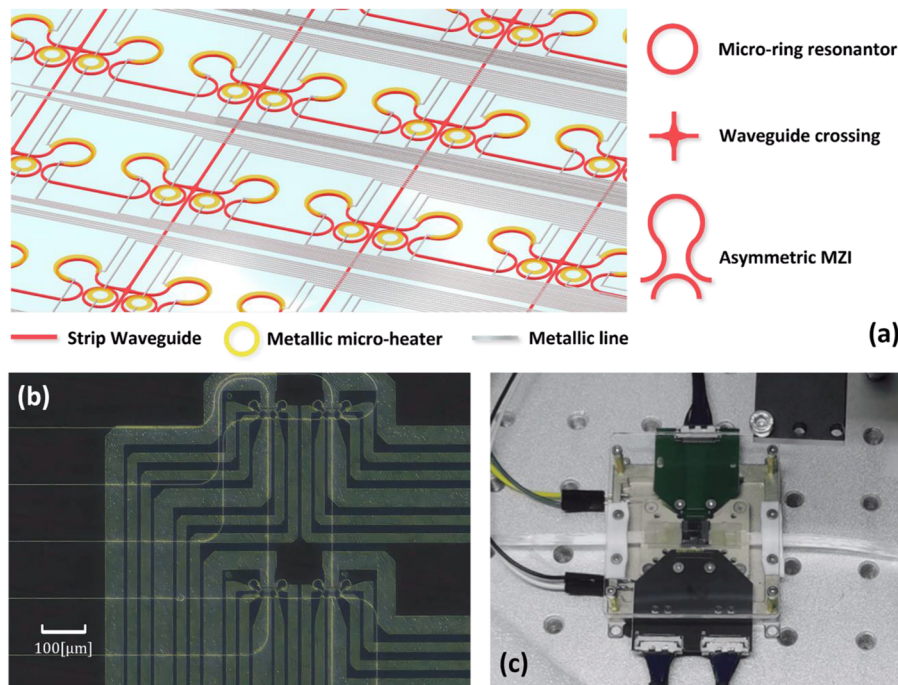
FIG. 4. Scalable photonic integrated AMZI-FPRA processor chip. (a) Schematic layout of the proposed AMZI-FPRA processor chip. (b) Microscope image of the 2 × 2 AMZI-FPRA processor chip. (c) Image of the chip package.

control signals utilizes TiW/Al bilayer material integrated with an oxide passivation layer through a three-layer heating metal process technique. Programmability is realized by utilizing the thermo-optic effect to tune the effective refractive index of the waveguide. As shown in Fig. 4(c), the device employs end-fire coupling technology, aligning the chip's end couplers with an array of standard optical fibers spaced at 127-μm intervals. For electrical control signal access, wire bonding technology is utilized to package the chip onto a printed circuit board. In addition, during the chip packaging, a temperature control system is implemented to prevent excessive heating that could potentially impact device performance. The effective area of the chip is $170 \times 84 \ \mu m^2$.

B. Tunable bandpass optical filtering

A bandpass optical filter enables the transmission of specific frequencies while effectively suppressing other signals. Tunable bandpass optical filters can be more effectively applied to microwave photonic signal processing scenarios. After programming, the proposed AMZI-FPRA can be configured as various types of bandpass optical filters. Figure 5 illustrates the transmission spectra obtained from port 2 when the input optical signal (provided by TSL-710, Santec) enters the processor through port 0 and is measured by the optical power meter (MPM-210, Santec). The inset in the inset shows the device schematic, where red labels indicate intrinsic waveguides and yellow labels indicate tuned positions. As shown in Fig. 5(a),

when the heating power reaches 12 mW, the central wavelength exhibits a red shift of 2.87 nm, thereby demonstrating the tunability of a central wavelength. In addition, Fig. 5(b) illustrates that simultaneous tuning of both the micro-ring and AMZI arm can result in a resonance peak change in 4.62 dB at a heating power of 37.50 mW, enabling its application as a filter with tunable-peak characteristics.

If two or more micro-rings are activated, the passband can be broadened and flattened through precise tuning. In our experiments, a flat-top filter is formed by applying DC voltages of 1.5 V (right side) and 1.604 V (left side) to two neighboring rings in the same cell. As shown in Fig. 5(c), when only one ring is activated, the optical filter exhibits a 3-dB bandwidth of 60 pm and an out-of-band rejection ratio of 24 dB over a bandwidth range of 1 nm at the central wavelength. Moreover, after reconstructing the flat-top filter, it demonstrates improved performance with a 1-dB bandwidth of 93 pm, a 3-dB bandwidth of 136 pm, an in-band ripple of only 0.88 dB, and an out-of-band rejection ratio of 16 dB over a range of ±0.5 nm around the central wavelength. In addition, by tuning the resonance wavelengths with the opposite micro-rings of adjacent cells, we can achieve an even richer variety of filter line shapes. Figure 5(d) illustrates that as heating power increases gradually, the spectral line shape transitions from Lorentzian to Fano or an electromagnetically induced transparent (EIT). Notably, the spectral resolution of the Fano line shape can be adjusted while maintaining a constant central wavelength. The Fano line shape holds great potential for applications in low-power optical switches, modulators, and high-sensitivity optical sensors. The linear region of its spectrum
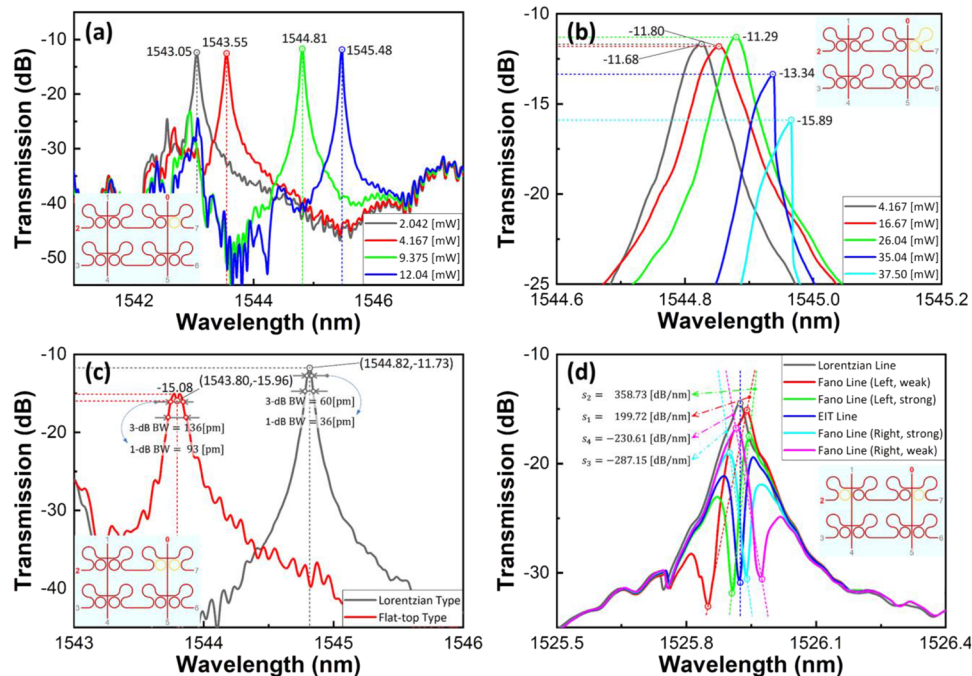
FIG. 5. 2×2 AMZI-FPRA reconfigured into a tunable optical bandpass filter. (a) Activation of a single ring to configure wavelength tunable narrowband filtering. (b) Activation of a single loop and its coupling region to configure bandpass peak tunable narrowband filtering. (c) Activation of two adjacent rings within the same cell to configure a flat-top filter. (d) Activation of two rings on opposite sides of the adjacent cell to configure Fano line and EIT line filters.

shows promise for expanding the application fields of the proposed chip.

C. Tunable bandstop optical filtering

The bandstop filter performs a complementary function to the bandpass filter, intercepting light of a particular wavelength while allowing others to pass through normally. The AMZI-FPRA proposed in this paper enables the implementation of band-stop optical filters with various types, depths, and bandwidths. Figure 6 illustrates the transmission spectra measured at port 5 when injecting the input optical signal into the processor through port 0. As shown in Fig. 6(a), activating a micro-ring allows for tuning the coupling coefficient of its coupling region, thereby facilitating the variation in notch depth. In addition, it can also be noticed that as the heating power reaches 37.50 mW, resulting in a steep slope, the spectrum transforms from its original Lorentzian line shape to an asymmetric Fano resonance-like line shape, exhibiting a notch depth of 14.25 dB, possibly attributed to the nonlinear effect of the micro-ring excited by high heating power. However, since using a single ring for varying notch depth tends to trigger distortion in spectral line patterns, another method is constructed, as shown in Fig. 6(b). By aligning multiple rings' resonance wavelengths, an increase in the final port's notch depth can be achieved while maintaining approximately Lorentzian line shapes for the filter and enlarging its 3-dB bandwidth with an increasing number of rings. Figure 6(c) demonstrates that the 3-dB bandwidth of the filter can be significantly broadened by staggering the resonance wavelengths of several micro-rings. By

ensuring a minimum notch depth of 5-dB, the bandstop spectrum formed by four rings achieves a bandwidth of 253 pm, nearly six times wider than that formed by a single ring (42 pm). In addition, the in-band ripple within the stopband is less than 1.66 dB. Figure 6(d) shows the redshift behavior of the bandstop filter. Taking an example of a composition with four rings, when a total power of 50.29 mW is applied to these rings, their central wavelength undergoes a redshift from the original 1543.74–1545.57 nm, spanning ~1.83 nm while maintaining similar notch depth levels. It can be observed that the bandwidth is reduced and the notch deepens. On one hand, as the bias voltage increases, it becomes more difficult to control the micro-ring due to the power being proportional to the square of the voltage, not to mention the inconsistent resistance of the heating electrodes. On the other hand, the power excites nonlinear effects in each ring, resulting in a narrower bandwidth and deeper notch.

D. Multichannel tunable fractional-order optical temporal differentiation

Optical temporal differentiators are widely used in various fields, such as optical processing and computation, pulse shaping, and optical sensing, to differentiate the complex envelope of an arbitrary input optical pulse in the time domain. By independently tuning the resonance wavelength of each micro-ring in the AMZI-FPRA, simultaneous optical temporal differential processing of multiple channels can be realized. Figure 7 presents the response results of the signal from port 4 to port 1, with a chip reconstruction
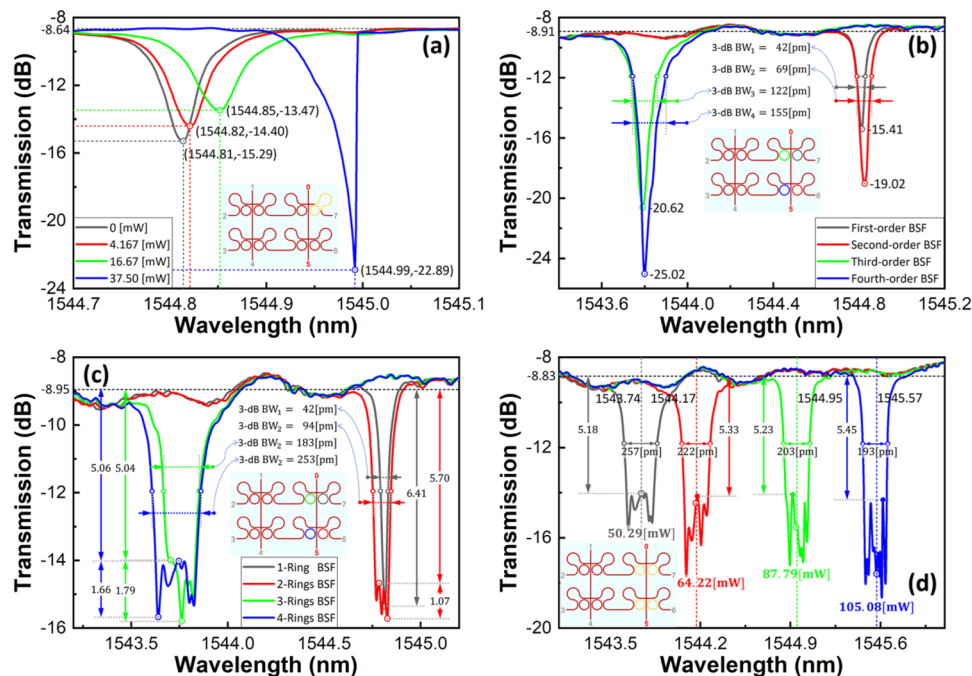
FIG. 6. 2 × 2 AMZI-FPRA reconfigured into a tunable optical band-stop filter. (a) Activating the coupling region of a single ring for bandstop notch depth tunable filtering. (b) Activating multiple rings to tune their resonance wavelengths for bandstop notch depth tunable filtering (micro-rings' colors represent the order in which they are involved in spectrum formation). (c) Activating multiple rings for bandwidth tunable filtering. (d) Activating multiple rings and tuning simultaneously for central wavelength variation.

17 June 2024 12:43:05

diagram shown in the inset in Fig. 7(b). The amplitude-frequency and phase-frequency curves are depicted in Figs. 7(a) and 7(b), respectively, which were measured using an optical vector network instrument (LUNA OVA5000) with different heating powers applied to the coupling region. It is observed that the phase response jumps from 0.366 to 1.326 rad. Depending on the experimental results, corresponding models were established using Lumerical INTERCONNECT software for simulating and demonstrating the differentiator function of the device. First, the wavelength of the input light should be adjusted to align precisely with the notches in different states, as shown in Fig. 7(a). As illustrated in Fig. 7(c), a deformation of the input Gaussian pulse can be observed with a full-width at half-maximum (FWHM) of about 7.87 ps. According to the phase change, it can be deduced that there has been a transition from a differential order n lower than the first order (0.12) to higher than the first order (1.58). The inset within Fig. 7(c) provides an enlarged view where spectral sidelobes can be observed, confirming both the differential phenomenon and a large jump in order, which may have resulted from an excessive tuning voltage step. Functionally, this result validates that a single ring within the array possesses tunable capabilities for temporal differentiation up to certain orders. Furthermore, multiple input signals can be simultaneously operated by invoking other rings. In addition, the alignment of resonance wavelengths among the rings enables the realization of higher order differential processing, thereby offering promising prospects for future tunable microwave-photonic signal processing.

E. Tunable microwave delay

The MRR exhibits strong optical confinement capability in the spectral notch, enabling different dispersion for various wavelengths. The compact footprint allows for a small microwave delay. By tuning the coupling coefficient with an AMZI, the proposed AMZI-FPRA can serve as a compact, tunable optical delay line. With the signal light propagating from port 1 to port 4, the delay spectrum is obtained and depicted in Fig. 8(a). At low heating power, anomalous dispersion occurs within a certain band. Considering the corresponding phase-frequency curves, the micro-ring exhibits an under-coupling resonance state with a steep drop in phase at the resonance wavelength, resulting in a delayed response. This phenomenon can be applied to the dispersion compensation of optical path transmission. As the heating power increases, there is a reduction in the anomalous dispersion phenomenon. When the power reaches 32.87 mW, an optical delay of 40.28 ps is achieved at 1554.49 nm, with a FWHM of 21.9 pm.

In addition, considering the correlation between the resonance state and the input port, the delay spectrum from port 3 to port 6
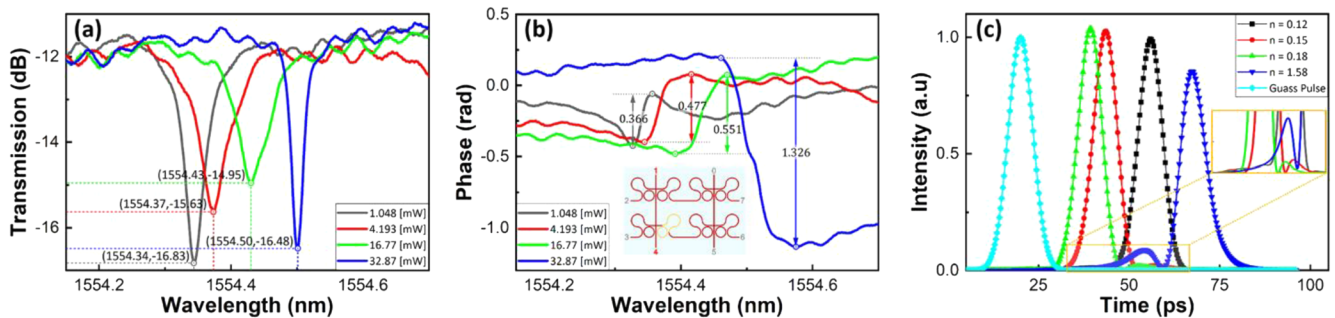
FIG. 7. 2 × 2 AMZI-FPRA reconfigured into a tunable fractional-order optical temporal differentiator. (a) Amplitude-frequency response changes when tuning the activated ring's coupling coefficients. (b) Phase-frequency response changes when tuning the activated ring's coupling coefficients. The inset shows the chip reconfiguration. (c) Differential output results of temporal signals at different orders. The inset shows the details of the temporal signals.
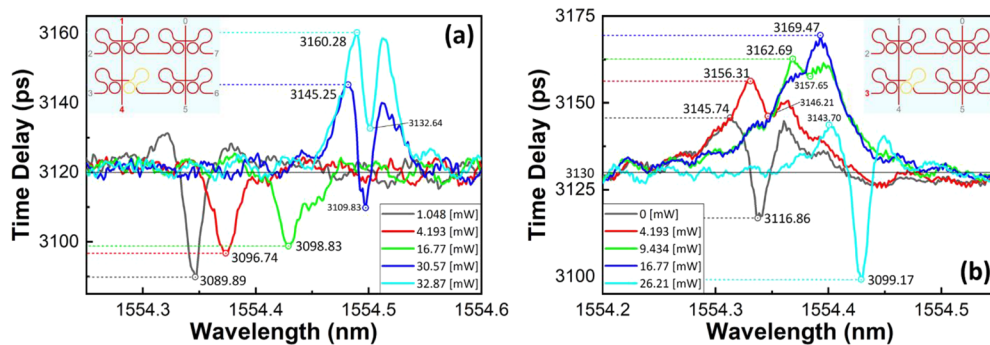
FIG. 8. 2 × 2 AMZI-FPRA reconstructed into a continuous tunable optical delay line. (a) Delay profile from port 1 to port 4. (b) Delay profile from port 3 to port 6.

is additionally tested. Compared with Fig. 8(a), the delay spectrum of this port exhibits a more pronounced up-convex delay profile. At a heating power of 16.77 mW, the delay reaches 30.47 ps with an operating bandwidth of 59.4 pm. Notably, when the power is 9.434 mW, the delay curve becomes approximately flat-top, exhibiting an operating bandwidth of 65.8 pm and a maximum delay of 32.69 ps. Since this delay line is regulated by a single ring's coupling coefficient, the delay change is continuous. Notably, when observing the deeper depression evident in the delay spectrum, it arises as a consequence of a phase change exceeding 2π. After reaching a phase change of 2π, there is an abrupt zigzag pattern observed at the center wavelength. To achieve longer delays or wider bandwidths, it is desirable to increase the number of rings involved in the reconfiguration. Actually, the optical delay demonstrated in the section is dependent on only one pathway of the chip. To further enhance its applicability, we can extend it to multiple pathways. After simultaneously introducing the light beams into multiple pathways, precise tuning of the resonance wavelengths and coupling coefficients can

be employed on different pathways. Therefore, a real-time delayed beam forming system will be established, which holds potential for application in phased-array antennas (PAAs).

F. Wavelength division (de)multiplexing and optical add-drop multiplexing

Wavelength division multiplexing (WDM) technology, being a crucial technology for enhancing communication capacity, is extensively employed in current optical communication networks. The proposed AMZI-FPRA not only enables the conventional functionality of WDM (DE)MUX but also offers channel spacing tunability with low power consumption, attributed to the high wavelength selectivity and wavelength tunability of micro-rings, as well as the coupling coefficient tunability of AMZI. An activation voltage of 1 V is applied to the micro-rings involved in the reconstruction during the test to ensure they are not overlapping with the wavelength of other rings. Figure 9(a) shows the schematic of the four-channel

FIG. 9. 2 × 2 AMZI-FPRA reconfigured for WDM. (a) Schematic of the optical path of the WDM with the micro-rings' colors corresponding to the spectral colors in (b). (b) Wavelength channel spacing tuning by applying different heating powers to the micro-rings.
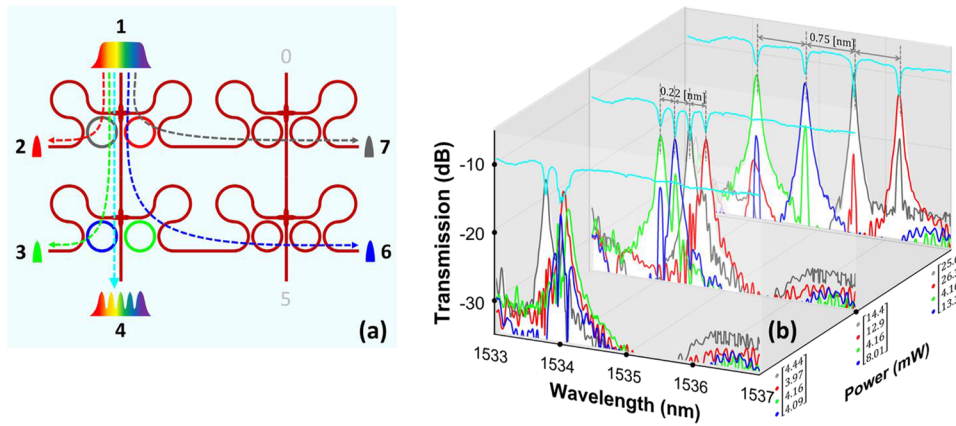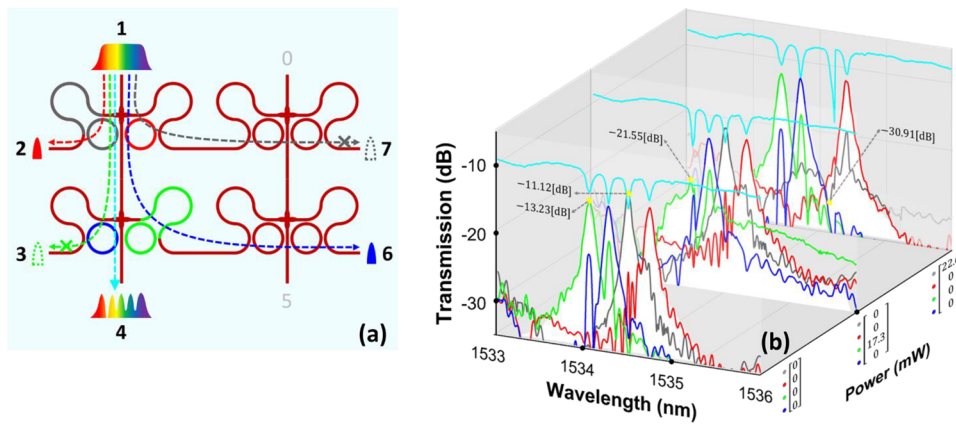

FIG. 10. 2 × 2 AMZI-FPRA reconfigured to OADM. (a) Schematic diagram of the optical path of the OADM with the micro-rings' colors corresponding to the spectral colors in (b). (b) Channel on–off control by applying different heating powers to the AMZI of the micro-rings.

WDM DEMUX optical path based on the reconfiguration of the 2 × 2 AMZI-FPRA. When signal light is input from port 1, specific wavelength signals can be selected and routed to desired ports by activating the resonant wavelengths of each micro-ring on pathways 1 to 4. The transmission spectra of drop ports 2, 3, 6, 7, and through port 4 are depicted in Fig. 9(b). By controlling the heating electrodes on the micro-rings, it is observed that the channel spacing increases from 0.22 to 0.75 nm while maintaining good consistency among channels. The normalized notch depth at the through port reaches a maximum value of 6 dB, and the normalized maximum peak value at the drop port is −2 dB. With a wavelength spacing of 0.22 nm, the total power consumption of the device is 39.47 mW. With a channel spacing as wide as 0.75 nm, the power consumption remains low at 69.36 mW.

Optical add-drop multiplexer (OADM) is based on WDM (DE)MUX, which enables the control of specific wavelength signals to achieve signal download and upload from the bus in the actual transmission link. This section demonstrates the basic functionality of the device as an OADM. As shown in Fig. 10(a), the schematic illustrates how a 2 × 2 AMZI-FPRA can be reconfigured into a four-channel OADM. By tuning the coupling coefficients of both the green ring and the gray ring, it becomes possible to control their on-off states. As shown in Fig. 10(b), the initial peak value of the green channel is −13.23 dB, with a channel spacing of 0.22 nm. When the heating power reaches 17.32 mW, the peak value of the corresponding channel is −21.55 dB, which can be considered a channel off state. Similarly, for the gray channel, its initial peak value is −11.12 dB. When the heating power reaches 22.61 mW, the peak value of the corresponding channel is −30.91 dB, which can also be regarded as a channel off state. Furthermore, continuous heating enables the reopening of these channels, while tuning facilitates increased channel peaks or enhanced inter-channel coherence, thereby enhancing fabrication tolerance. By further scaling up chip size, it becomes feasible to realize WDM systems that can accommodate more channels. As shown in Fig. 2(b), 40 channels with 0.22 nm channel spacing can be accommodated at an FSR of 9 nm, which demonstrates high potential for application and will play an important role in future high-speed photonic networks.

IV. DISCUSSION AND CONCLUSION

In summary, this paper proposes, fabricates, and experimentally tests an AMZI-FPRA signal processor based on a SOI optical platform. It successfully demonstrates the role of this AMZI-FPRA signal processor in the generation and processing of advanced microwave photonic signals. The processor depends on a two-dimensional square mesh structure with dual-tunability in resonance wavelength and resonance state. Compared to the FPDA, the footprint of our unit structure (85×42 μm^2) is larger but remains within the same order of magnitude. By introducing an AMZI structure, we transform the micro-disk's single-tunability into a micro-ring's dual-tunability in both resonance wavelength and resonance state. This greatly enhances the plasticity of a single component and further expands the functionality of the extended arrays. On one hand, in contrast to the MZI-based optical processor architecture, the reported structure is significantly larger than that of the proposed

device. In addition, the MZI-based architecture relies on meshing to achieve reconfigurability, whether it is a triangular, square, or hexagonal mesh. Consequently, the overall footprint will approach square centimeters in size. Despite a few area-optimization schemes that have been proposed, the integration problem of the MZI-based processor remains intractable. On the other hand, although this paper proposes fewer reconfigurable functions for an MZI-based architecture,[28] the unit and its array device proposed here can complement the functional limitations of an MZI-based optical processor, which possesses greater application value. Table I provides a summary of recent developments concerning reconfigurable optical processors. It can be seen that the device proposed in this paper achieves a better balance of area and functionality, and it can be efficiently implemented to route, store, and process optical signals. By programming each basic unit structure accordingly, various microwave photonic processing functions can be achieved. Furthermore, with an expansion in array size, the resulting processor will have more functions and better performance.

The nonlinear and temperature-sensitive characteristics of the proposed device result in performance distortion at high heating power and thermal crosstalk problems. To achieve better performance and functional characterization of the array devices, further optimization of single cell performance is required, including tunability, optical crosstalk, and environment robustness. For tunability purposes, a more rational design of coupling gaps is needed to ensure that the coupling state can traverse from under-coupling to over-coupling for different application scenarios. To suppress optical crosstalk caused by mode mismatch in the coupling region, the coupling between different waveguide types needs to be cautious, such as using Eulerian bending for the coupling region between the ring and the straight waveguide. Finally, for addressing thermal crosstalk issues and ambient temperature sensitivity, a more efficient temperature control system is necessary for ensuring chip operation stability within general environmental conditions. In addition to incorporating air slots to inhibit heat conduction, low heat-generating modulation methods such as depletion electro-optical modulators, micromechanics, or phase-change materials can be utilized to avoid heat generation, thereby eliminating thermal crosstalk.

In conclusion, we have successfully designed, fabricated, and characterized a silicon photonic AMZI-FPRA signal processor. Furthermore, we have demonstrated the effectiveness of using the AMZI-FPRA for advanced microwave signal generation and processing. Several important microwave photonic signal processing functions have been experimentally demonstrated by extending the cell structure into a 2 × 2 AMZI-FPRA signal processor, including optical bandpass filters with wavelength, peaks, and types tunable, optical bandstop filters with wavelength and bandwidth tunable, multichannel fractional-order tunable optical temporal differentiators, tunable microwave delays, as well as reconfigurable WDM (DE)MUX and OADM.

The simple mesh structure of the processor enables further extensive expansion, offering enhanced functions as well as improved performance for programmable photonic signal processing, such as optical pulse shapers, beam forming, and PAA. The chip holds immense potential for applications in fields including communications, biophotonics, sensing, multiprocessor interconnections, switching, and quantum information. This work represents an

<div style="text-align: right">17 June 2024 12:43:05</div>

TABLE I. Comparison of reported programmable photonic circuits.

Year	References	Material platform	Mesh architecture	Unit type	Chip size (mesh number)	Reported functionality
2015	27	Si_3O_4	Square recirculating	MZI	3.5×8.5 mm^2 (2)	- Notch filter - Hilbert transformer, - Bandpass filter, - Delay line - Unbalanced FIR Mach–Zehnder filters - Ring cavities - Complex CROW
2017	28	SOI	Hexagonal recirculating	MZI	15×15 mm^2 (7)	- SCISSOR - Ring-assisted MZI filters - Multiple input–multiple output linear-optic transformation devices, −21 functionalities in report
2019	38	Si_3O_4	Triangular recirculating	DD-DC	2.5×7.2 mm^2 (2)	- Single ring resonator - Series double-ring resonator - Wavelength Demultiplexer - Flat-top filter
2020	44	SOI	Square feedforward	MDR	0.4×0.4 mm^2 (16)	- Tunable delay line - Differentiator - Beamforming network - Optical pulse shaper
2021	41	SOI	Cascaded feedforward	MDC	12.2×3.6 mm^2 (1)	- Arbitrary transmission matrix reconstruction (different polarization) - Reconfigurable optical splitters - Reconfigurable optical filters
2021	51	Si_3N_4	Hexagonal recirculating	MZI	5.5×11 mm^2 (10)	- Reconfigurable microwave photonic filters - Digital signal transmission
2023	52	SOI	Rectangular feedforward	PBW[a]	0.1×0.25 mm^2 (5)	- Reconfigurable optical 4×4 matrix multiplication - Arbitrary optical 4×4 beam splitting - Lorentzian and flat-top bandpass filter - Fano resonance filter and EIT filter - Tunable bandstop filter
2024	Our work	SOI	Square feedforward	AMZI-MRR	0.17×0.08 mm^2 (4)	- Continuously tunable delay line - Fraction-order-tunable optical differentiator - Wavelength Demultiplexer - Optical add-drop multiplexer

[a]Periodic bimodal waveguides, PBW.

important step toward realizing a new paradigm of multipurpose reconfigurable photonic processors.

AUTHOR DECLARATIONS

Conflict of Interest

The authors have no conflicts to disclose.

Author Contributions

Yaohui Sun: Conceptualization (lead); Data curation (lead); Formal analysis (lead); Methodology (lead); Project administration (equal); Software (lead); Validation (lead); Visualization (lead); Writing – original draft (lead); Writing – review & editing (equal). **Dongyu Wang**: Investigation (equal); Methodology (equal); Software (equal); Visualization (equal); Writing – review & editing (equal). **Lihan Wang**: Methodology (equal); Resources (equal); Software (equal); Validation (equal). **Yue Zhou**: Data curation (supporting); Methodology (supporting); Supervision (supporting); Writing – review & editing (supporting). **Shilong Pan**: Funding acquisition (supporting); Investigation (supporting); Resources (supporting); Software (supporting). **Guohua Hu**: Funding acquisition (lead); Investigation (lead); Project administration (equal); Resources (lead); Supervision (equal); Writing – review & editing (equal). **Binfeng Yun**: Funding acquisition (supporting); Resources (supporting). **Yiping Cui**: Investigation (supporting); Resources (supporting).

DATA AVAILABILITY

The data that support the findings of this study are available from the corresponding author upon reasonable request.

REFERENCES

[1] C.-W. Tsai, C.-F. Lai, H.-C. Chao, and A. V. Vasilakos, J. Big Data **2**(1), 21 (2015).

[2] T. Zheng, G. Chen, X. Wang, C. Chen, X. Wang, and S. Luo, Sci. China Inf. Sci. **62**(8), 82101 (2019).

[3] M. Li and N. Zhu, Front. Optoelectron. **9**(2), 160–185 (2016).

[4] J. Capmany and D. Novak, Nat. Photonics **1**(6), 319–330 (2007).

[5] J. Yao, in paper Presented at the 16th Opto-Electronics and Communications Conference, 2011.

[6] J. Azaña and L. R. Chen, J. Opt. Soc. Am. B **19**(11), 2758–2769 (2002).

[7] J. Yao and J. Capmany, Sci. China Inf. Sci. **65**(12), 221401 (2022).

[8] H. J. Caulfield and S. Dolev, Nat. Photonics **4**(5), 261–263 (2010).

[9] D. Perez, I. Gasulla, J. Capmany, and R. A. Soref, Opt. Express **24**(11), 12093–12106 (2016).

[10] R. A. Minasian, in paper Presented at the 2020 International Topical Meeting on Microwave Photonics (MWP), 2020.

[11] C.-Y. Fang, H.-H. Lin, M. Alouini, Y. Fainman, and A. El Amili, Sci. Rep. **9**(1), 11166 (2019).

[12] J. Capmany, J. Mora, I. Gasulla, J. Sancho, J. Lloret, and S. Sales, J. Lightwave Technol. **31**(4), 571–586 (2013).

[13] D. A. B. Miller, Nat. Photonics **11**(7), 403–404 (2017).

[14] Y. Shen, N. C. Harris, S. Skirlo, M. Prabhu, T. Baehr-Jones, M. Hochberg, X. Sun, S. Zhao, H. Larochelle, D. Englund, and M. Soljačić, Nat. Photonics **11**(7), 441–446 (2017).

[15] N. C. Harris, G. R. Steinbrecher, M. Prabhu, Y. Lahini, J. Mower, D. Bunandar, C. Chen, F. N. C. Wong, T. Baehr-Jones, M. Hochberg, S. Lloyd, and D. Englund, Nat. Photonics **11**(7), 447–452 (2017).

[16] X. Lin, Y. Rivenson, N. T. Yardimci, M. Veli, Y. Luo, M. Jarrahi, and A. Ozcan, Science **361**(6406), 1004–1008 (2018).

[17] J. Sancho, J. Bourderionnet, J. Lloret, S. Combrié, I. Gasulla, S. Xavier, S. Sales, P. Colman, G. Lehoucq, D. Dolfi, J. Capmany, and A. De Rossi, Nat. Commun. **3**(1), 1075 (2012).

[18] M. Ferrera, Y. Park, L. Razzari, B. E. Little, S. T. Chu, R. Morandotti, D. J. Moss, and J. Azaña, Nat. Commun. **1**(1), 29 (2010).

[19] D. Zhang, X. Feng, X. Li, K. Cui, F. Liu, and Y. Huang, J. Lightwave Technol. **31**(23), 3668–3675 (2013).

[20] R. L. Moreira, J. Garcia, W. Li, J. Bauters, J. S. Barton, M. J. R. Heck, J. E. Bowers, and D. J. Blumenthal, IEEE Photonics Technol. Lett. **25**(12), 1165–1168 (2013).

[21] Q. Sun, L. Zhou, L. Lu, G. Zhou, and J. Chen, IEEE Photonics J. **10**(6), 1–12 (2018).

[22] W. Liu, M. Li, R. S. Guzzon, E. J. Norberg, J. S. Parker, M. Lu, L. A. Coldren, and J. Yao, Nat. Photonics **10**(3), 190–195 (2016).

[23] D. Liang, J. Capmany, D. Perez, P. Dasmahapatra, Q. Tan, X. Li, L. Li, and Y. Liu, IEEE Photonics J. **13**(1), 6600911 (2021).

[24] P. Zheng, X. Xu, G. Hu, R. Zhang, B. Yun, and Y. Cui, J. Lightwave Technol. **39**(5), 1429–1437 (2021).

[25] Y. Sun, C. Deng, Z. Xie, L. Huang, G. Hu, B. Yun, and Y. Cu, Opt. Commun. **542**, 129546 (2023).

[26] W. Zhang, L. Zhou, Y. Xu, Z. Zhao, and S. Zheng, J. Lightwave Technol. **40**(22), 7375–7382 (2022).

[27] L. Zhuang, C. G. H. Roeloffzen, M. Hoekman, K.-J. Boller, and A. J. Lowery, Optica **2**(10), 854 (2015).

[28] D. Pérez, I. Gasulla, L. Crudgington, D. J. Thomson, A. Z. Khokhar, K. Li, W. Cao, G. Z. Mashanovich, and J. Capmany, Nat. Commun. **8**(1), 636 (2017).

[29] W. Bogaerts, D. Perez, J. Capmany, D. A. B. Miller, J. Poon, D. Englund, F. Morichetti, and A. Melloni, Nature **586**(7828), 207–216 (2020).

[30] X. Cao, S. Zheng, Y. Long, Z. Ruan, Y. Luo, and J. Wang, ACS Photonics **7**(10), 2658–2675 (2020).

[31] D. Perez-Lopez, A. Lopez, P. DasMahapatra, and J. Capmany, Nat. Commun. **11**(1), 6359 (2020).

[32] Y. Yao, Y. Zhao, and J. Dong, Proc. SPIE **11902**, 1190215 (2021).

[33] J. Wu, T. Moein, X. Xu, and D. J. Moss, APL Photonics **3**(4), 046102 (2018).

[34] H. Arianfard, J. Wu, S. Juodkazis, and D. J. Moss, J. Lightwave Technol. **39**(5), 1400–1408 (2021).

[35] L. Lu, L. Shen, W. Gao, L. Zhou, and J. Chen, IEEE Photonics J. **11**(6), 6603312 (2019).

[36] S. Pan, Z. Tang, M. Huang, and S. Li, IEEE J. Sel. Top. Quantum Electron. **26**(5), 7701712 (2020).

[37] R. Tang, T. Tanemura, and Y. Nakano, IEEE Photonics Technol. Lett. **29**(12), 971–974 (2017).

[38] D. Pérez-López, A. M. Gutierrez, E. Sánchez, P. DasMahapatra, and J. Capmany, Opt. Express **27**(26), 38071–38086 (2019).

[39] Z. Cheng, J. Dong, and X. Zhang, Opt. Lett. **45**(8), 2363–2366 (2020).

[40] R. Soref, F. De Leonardis, and V. M. N. Passaro, Opt. Express **29**(6), 8751–8762 (2021).

[41] R. Tang, R. Tanomura, T. Tanemura, and Y. Nakano, ACS Photonics **8**(7), 2074–2080 (2021).

[42] D. Yi, Y. Wang, and H. K. Tsang, APL Photonics **6**(10), 100801 (2021).

[43] D. Yi, Y. Zhang, H. K. Tsang IEEE, in paper presented at the IEEE Photonics Conference (IPC), San Antonio, TX, 2019.

[44] W. Zhang and J. Yao, Nat. Commun. **11**(1), 406 (2020).

[45] W. Bogaerts, P. De Heyn, T. Van Vaerenbergh, K. De Vos, S. Kumar Selvaraja, T. Claes, P. Dumon, P. Bienstman, D. Van Thourhout, and R. Baets, Laser Photonics Rev. **6**(1), 47–73 (2012).

[46] Z. Ying, Z. Wang, Z. Zhao, S. Dhar, D. Z. Pan, R. Soref, and R. T. Chen, Appl. Phys. Lett. **112**(11), 111108 (2018).

[47] L. Xu, Y. Yu, X. Liu, X. Shu, and X. Zhang, ACS Photonics **8**(11), 3156–3161 (2021).

[48] M. Liu, Y. Zhao, X. Wang, X. Zhang, S. Gao, J. Dong, and X. Cai, Opt. Express **25**(26), 33305–33314 (2017).

[49] Y. Zhao, X. Wang, D. Gao, J. Dong, and X. Zhang, Front. Optoelectron. **12**(2), 148–156 (2019).

[50] Y. Liu, C. Wu, X. Gu, Y. Kong, X. Yu, R. Ge, X. Cai, X. Qiang, J. Wu, X. Yang, and P. Xu, Opt. Lett. **45**(1), 73–76 (2020).

[51] D. Pérez-López, A. Gutiérrez, and J. Capmany, Opt. Express **29**(6), 9043–9059 (2021).

[52] L. Torrijos-Morán, D. Pérez-Galacho, and D. Pérez-López, Laser Photonics Rev. **18**, 2300505 (2023).

17 June 2024 12:43:05